

Optimizing Electric Propulsion Systems for Unmanned Aerial Vehicles

Ohad Gur* and Aviv Rosen†

Technion—Israel Institute of Technology, Haifa 32000, Israel

DOI: 10.2514/1.41027

Design of an electric propulsion system for an unmanned aerial vehicle incorporates various disciplines such as the propeller’s aerodynamic and structural properties, characteristics of the electric system, and characteristics of the vehicle itself. This makes the design of this propulsion system a multidisciplinary design optimization task. Although the present propeller model is based on previous derivations that are described very briefly, new models of the electric motor and battery pack, which are based on examining existing products on the market, are described in more detail. The propeller model and a model of the electric system, together with various optimization schemes, are used to design optimal propulsion systems for a mini unmanned aerial vehicle for various goals and under various constraints. Important design trends are presented, discussed, and explained. Although the first part of the investigation is based on typical characteristics of the electric system, the second part includes a sensitivity study of the influence of variations of these characteristics on the optimal system design.

Nomenclature

B_{E_B}	=	battery energy density
B_{I_0}	=	no-load current parameter
B_{K_V}	=	motor speed-constant parameter
B_{P-M}	=	maximum power-to-mass ratio
B_{R_a}	=	internal-resistance parameter
C_{D, C_L}	=	vehicle’s drag and lift coefficients
C_d	=	blade cross-sectional drag coefficient
$C_{L\max}$	=	vehicle’s maximum lift coefficient
c	=	chord
E_B	=	battery energy capacity
g	=	gravity acceleration
K_V	=	motor speed constant
I_{in}	=	driver input current
I_0	=	motor no-load current
m_B	=	battery-pack mass
m_M	=	electric motor mass
M_{tip}	=	blade tip Mach number
m_{total}	=	total vehicle mass
m_0	=	vehicle mass without the propulsion system
P_{in}	=	electric system input power
P_{out}	=	motor output power
$P_{out-max}$	=	maximum motor output power
R	=	propeller radius
R_a	=	motor resistance
r	=	radial coordinate
S_W	=	wing area
T	=	thrust
t	=	cross-sectional thickness
V_F	=	airspeed
V_{in}	=	driver input voltage
V_l	=	loitering airspeed
V_{st}	=	stall airspeed

W_a	=	axial induced velocity
η_D	=	driver efficiency
η_P	=	propeller efficiency
$\eta_{P-ideal}$	=	ideal propeller efficiency
η_S	=	electric system efficiency
ρ_a	=	air density
$\bar{\sigma}$	=	maximal von Mises stress
Ω	=	rotational speed

I. Introduction

MOST of today’s unmanned aerial vehicles (UAVs) are used for reconnaissance and surveillance missions [1]. Considerable effort has been directed toward the development of small tactical UAVs, sometimes referred to as mini or micro UAVs [2,3]. These vehicles are applied as tactical surveillance tools, used by soldiers for “behind the hill” reconnaissance purposes. Most of these UAVs are equipped with electric motors that contribute to the simplicity of operation and significantly reduce their noise signature.

The propulsion systems of these small UAVs (batteries, motor, propeller, etc.) account for as much as 60% of the vehicle weight [4]. Therefore, optimization of the propulsion systems is extremely crucial.

The electric propulsion system of a typical UAV includes the following components: propeller; electric motor; energy source; gear box (optional); driver; wiring, plugs, and connectors; and cooling system (optional).

The paper will concentrate on the first three items (propeller, electric motor, and the batteries). Although the other components are important, the influence of the first three on the UAV’s performance is usually far more significant.

Most of the existing methods for propeller design are based on the well-known work of Betz [5] from 1919. An example of such a design is presented in [6]. This approach is based on optimizing the propeller’s geometry at a certain specific operating condition (a certain combination of airspeed, altitude, and propeller rotational speed), such that the power, which is required to obtain a certain propulsive force at these operating conditions, is minimized (or, alternatively, the thrust produced by a certain power is maximized). An example of such a design is the propeller of Rutan’s Voyager (the first nonstop, nonrefueled flight around the world) [7].

The Betz method considers only the aerodynamic efficiency of the propeller. It does not include structural considerations or the propeller’s noise signature. Thus, for practical design of a propeller when using the Betz method, a serial design process is used. First, the optimal aerodynamic propeller, having a maximum efficiency, is

Presented as Paper 5916 at the 12th AIAA/ISSMO Multidisciplinary Analysis and Optimization Conference, Victoria, British Columbia, Canada, 10–12 September 2008; received 15 September 2008; accepted for publication 31 March 2009. Copyright © 2009 by the American Institute of Aeronautics and Astronautics, Inc. All rights reserved. Copies of this paper may be made for personal or internal use, on condition that the copier pay the \$10.00 per-copy fee to the Copyright Clearance Center, Inc., 222 Rosewood Drive, Danvers, MA 01923; include the code 0021-8669/09 and \$10.00 in correspondence with the CCC.

*Researcher, Faculty of Aerospace Engineering; ohadg@aerodyne.technion.ac.il. Member AIAA.

†Professor, Faculty of Aerospace Engineering; rosen@aerodyne.technion.ac.il. Fellow AIAA.

defined. Then this propeller is modified to fulfill other goals. Such a process has been used extensively [7–9]. The main disadvantage of such an iterative process is that it does not ensure that the final design will be optimal.

The best approach for the complex design of propellers is to use multidisciplinary design optimization (MDO) [10,11]. During MDO, all of the different design goals and constraints are addressed simultaneously. Thus, the best compromise between contradictory design goals will be reached. This kind of approach has been already applied to rotary wing designs. Most of the previous investigations were limited to two disciplines: either aerodynamic and structural analyses, mostly for helicopter rotors [12,13], or aerodynamic and acoustic design of propellers [14–19]. Most of the previous investigations used a very limited number of design variables, rather than the full range of design parameters that are under the authority of the designer. Previous investigations also included a limited number of constraints and did not consider the entire propulsion system (namely, the coupled system: propeller, gearbox, engine, and energy source). For example, [20] does not take into account the engine characteristics during the propeller design. Only after the isolated propeller optimization are these characteristics used to calculate the performance of the entire propulsion system, which is the measure of the design quality. Recently, a new comprehensive MDO design tool for propeller-based propulsion systems was presented by the authors that offers a very high flexibility in choosing the cost function, design variables, and constraints [21,22].

The design of various electric mini UAVs has been described in the past [3,4,23–30]. Most of these papers discuss the design considerations of the various components and the integration of these components into the final design.

It is clear from previous studies on electric UAVs, as well as other propeller-based propulsion systems, that an optimization of the electric propulsion system of a UAV should include a simultaneous consideration of the: propeller, electric motor, and battery. The performance and characteristics of the vehicle depend on the strong interaction between these three.

The purpose of the present study is not to present an optimal design of a specific electric propulsion system for a certain UAV, but rather to investigate trends and obtain insight into the interactions between the various components of the system. To do that, theoretical models of these components are required. Although the propeller model of the present study is based on the well-known blade-element/momentum theory, special effort is directed into modeling the electric motor and battery. These models are based on a comprehensive investigation of existing motors and batteries, followed by derivations of representative models that include certain parameters. All the various models are combined with various optimization schemes to form a comprehensive MDO tool that can handle a large number and variety of design variables and constraints. There is also a large flexibility in choosing the cost function: namely, the goal of the design.

The new MDO tool is used to study optimal propulsion systems for different design goals (cost functions) and constraints. The interactions between the various components of the system are investigated, explained, and discussed.

As indicated previously, the analytical models of the electric motor and battery represent typical existing technologies. Yet these technologies exhibit significant variations between products and a continuous rate of improvement. Thus, the paper also includes a sensitivity study to understand how variations in the characteristics of the various electric components can affect the system optimal design.

II. Analysis Tools

The following analysis tools are used to model the components of the entire propulsion system: propeller's aerodynamic model, propeller's structural model, electric motor model, and battery model. The selection of each model is based on the following two considerations:

- 1) It should be sufficiently accurate.
- 2) It should be efficient, because the optimization procedure includes a very high number of iterations.

The aerodynamic model calculates the distribution of the aerodynamic loads along the propeller blades. These data are used to calculate the propeller's thrust and required power. In addition, the distribution of the aerodynamic loads is used as an input for the structural analysis. In the present case, a momentum/blade-element model is used. For regular flight conditions of propellers (uniform axial flow at high-enough advance ratios), the blade's cross sections do not experience stall and the momentum/blade-element model gives results of good accuracy [31]. The blade-element/momentum analysis can be extended to include the influence of rotation on the aerodynamic behavior of cross sections experiencing stall [32]. Momentum/blade-element models are usually much more efficient than other models; thus, they are suitable for the present purpose.

A structural analysis is essential to ensure that the propeller blades will be able to withstand the aerodynamic and inertial loads that act along them. Common tools for the structural analysis of blades are finite element models [33]. To reduce the computations, a more efficient rod model, together with a transfer-matrix formulation, is used [34].

The rod structural model describes the propeller blades as a series of straight segments located along the blade's elastic axis. The structural cross-sectional properties are uniform along each segment and equal to the structural properties of a representative cross section of that segment. The transfer-matrix formulation is applied using the boundary conditions of a cantilevered rod (clamped root and free tip). The solution procedure is very efficient and the results are very accurate [34].

A. Electric Motor Model

Characteristics of 250 brushless direct-current electric motors were analyzed. Data for these motors were taken from various Web-based catalogs.[‡] The list includes 12 manufacturers that are divided into three main groups:

- 1) Group I contains the manufacturers of heavy-duty/high-voltage electric motors.
- 2) Group II contains the manufacturers of high-performance industrial electric motors.
- 3) Group III contains the manufacturers of aeromodel/hobby electric motors.

Heavy-duty motors are characterized by low speed and high torque. On the other hand, aeromodel motors exhibit high speed and low torque.

There is a relation between a motor maximum output power and its size/weight [35]. Figure 1 presents the motors' maximum continuous power $P_{\text{out-max}}$ versus their mass m_M . Each manufacturer is presented by a different symbol (there are 12 different symbols). In addition, each symbol indicates to which group (of the aforementioned three groups) this manufacturer belongs:

- 1) The heavy-duty group uses solid symbols.
- 2) The high-performance group uses open symbols.
- 3) The aeromodel group uses + or × symbols.

Figure 1 also presents representative boundaries between these three groups. Heavy-duty motors exhibit a low power-to-weight ratio, whereas aeromodel motors exhibit a high power-to-weight ratio. It is the goal of any air vehicle to exhibit a high power-to-weight ratio, and thus aeromodel motors are natural candidates for UAV applications. Yet UAV motors are required to present much better reliability and endurance than hobby motors. This aspect, as well as experience with existing UAV motors, leads to the conclusion that group II is a better representative of UAV motors.

The motor model of the present study will assume a constant maximum power-to-mass ratio B_{P-M} [35]:

$$P_{\text{out-max}} = B_{P-M} \cdot m_M \quad (1)$$

In group II, B_{P-M} varies between the following limits:

[‡]Data available online at <http://www.bental.co.il/>, <http://www.alliedmotion.com/>, <http://www.micromo.com/>, <http://www.cyclone-usa.com/>, and <http://www.maxonmotorusa.com/> [retrieved 15 March 2009].

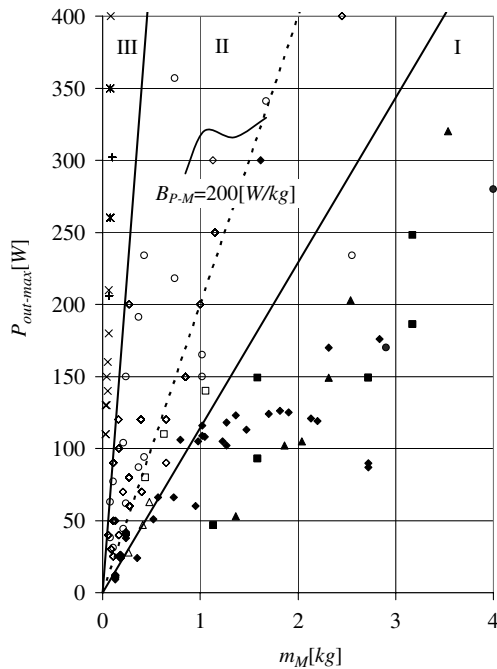


Fig. 1 Motor maximum output power as a function of motor mass.

$$110 \text{ W/kg} < B_{P-M} < 800 \text{ W/kg} \quad (2)$$

Equation (2) presents a very wide range of variation of B_{P-M} . Examination of the data in Fig. 1 shows that for a certain series of products from the same manufacturer, different sizes of motors follow Eq. (1).

The differences in B_{P-M} between manufacturers, or between different series of the same manufacturer, probably emerge from different technologies, design concepts, or manufacturing methods. For the present study, a typical value of $B_{P-M} = 200 \text{ W/kg}$ will be used.

During the present study, electric motors will be described by a simple performance model [36], which is based on the following assumptions:

- 1) Power factor is equal to unit. This assumption is applicable to small brushless permanent-magnet motors [37].
- 2) Magnetic losses (eddy/Foucault current and magnetic hysteresis) can be neglected.

Using these assumptions, the driver input power P_{in} and shaft output power P_{out} are given by the following expressions:

$$P_{in} = V_{in} \cdot I_{in} \quad (3)$$

$$P_{out} = (I_{in} - I_0) \cdot (V_{in} - I_{in} \cdot R_a) \quad (4)$$

where I_{in} is the driver's input current, V_{in} is the driver's input voltage, I_0 is the current at zero load, and R_a is the motor resistance.

The electric system efficiency η_S is

$$\eta_S = \eta_D \cdot \left(1 - \frac{I_{in} \cdot R_a}{V_{in}}\right) \cdot \left(1 - \frac{I_0}{I_{in}}\right) \quad (5)$$

where η_D is the driver efficiency. In the present study, the driver efficiency is considered to be constant: $\eta_D = 0.95$. The following relation also exists:

$$\Omega = (V_{in} - I_{in} \cdot R_a) \cdot K_V \quad (6)$$

where Ω is motor rotational speed and K_V is motor speed constant, which is identical to the inverse of torque constant or the inverse of the back electromotive force constant.

The preceding described simplified model includes the following three motor parameters: speed constant K_V , internal resistance R_a , and no-load current I_0 . Simple relations between these three

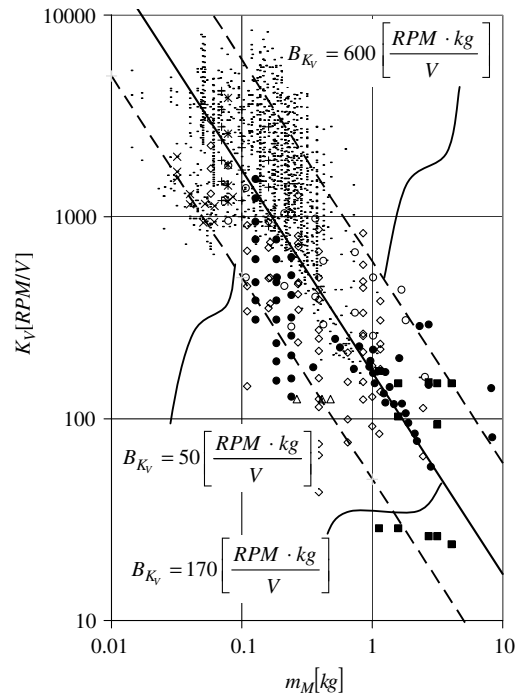


Fig. 2 Speed constant as a function of motor mass.

parameters will be used. These relations are based on available motor data (see footnote [‡]).

The motor speed constant K_V is directly related to the motor size. The torque constant (inverse of speed constant) depends on the motor flux linkage and magnetic circuit: the larger the motor, the larger the flux linkage and torque constant. Consequently, as the rotor becomes heavier, the speed constant decreases. Figure 2 presents motor speed constant versus motor mass for all the motors that were shown in Fig. 1. Figure 2 also includes a database of electric aeromodel motors.[‡] This database contains data for about 1300 electric motors, which are mostly shown as a cloud of dots on the upper left side of the figure.

As indicated previously, as motors become lighter, their speed constants become higher (heavy-duty motors have low speed constants); thus, a general relation can be described as follows:

$$K_V \text{ rpm/V} = B_{K_V} / m_M \text{ kg} \quad (7)$$

where B_{K_V} is a speed-constant parameter. For most cases, it falls between the following values (see Fig. 2):

$$50 \text{ rpm} \cdot \text{kg/V} < B_{K_V} < 600 \text{ rpm} \cdot \text{kg/V} \quad (8)$$

For the present study, a typical value of $B_{K_V} = 170 \text{ rpm} \cdot \text{kg/V}$ will be used (see Fig. 2).

Motor resistance versus motors speed constants is shown in Fig. 3. The following trend is clear: small aeromodel motors have low resistance, and heavy-duty motors exhibit high resistance. In the present study, the following relation is used (see Fig. 3):

$$R_a \Omega = \frac{B_{R_a}}{[K_V \text{ rpm/V}]^2} \quad (9)$$

where B_{R_a} is the internal-resistance parameter that, for most cases, changes between the following values (see Fig. 3):

$$2500 \text{ V}^2 \cdot \Omega / \text{rpm}^2 < B_{R_a} < 1 \times 10^6 \text{ V}^2 \cdot \Omega / \text{rpm}^2 \quad (10)$$

For the present study, a typical value of $B_{R_a} = 60,000 \text{ V}^2 \cdot \Omega / \text{rpm}^2$ will be used (see Fig. 3).

[‡]Data available online at <http://www.motocalc.com/> [retrieved 15 March 2009].

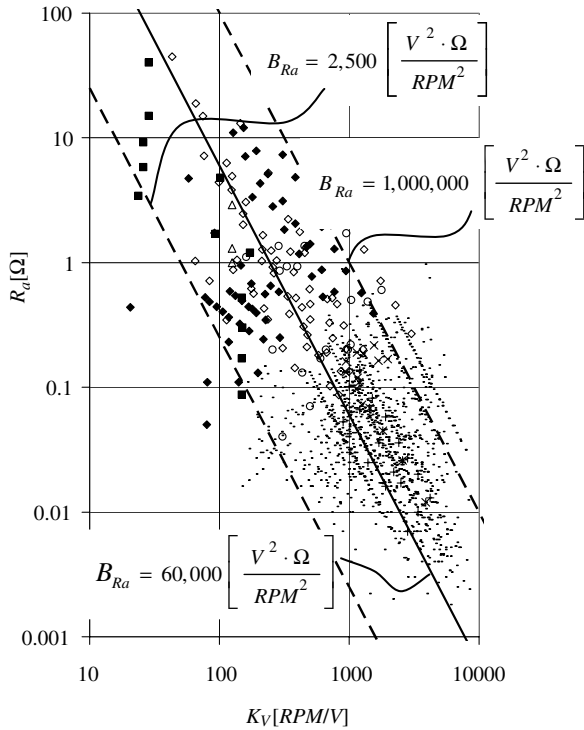


Fig. 3 Internal resistance as a function of speed coefficient.

In the same manner, Fig. 4 presents motors no-load current I_0 versus motor resistance R_a . The following representative relation is used in the present study:

$$I_0 \text{ A} = \frac{B_{I_0}}{(R_a \Omega)^{0.6}} \quad (11)$$

where B_{I_0} is the no-load current parameter that, for most cases, changes between the following values (see Fig. 4):

$$0.1 \text{ A} \cdot \Omega^{0.6} < B_{I_0} < 0.4 \text{ A} \cdot \Omega^{0.6} \quad (12)$$

For the present study, a typical value of $B_{I_0} = 0.2 \text{ A} \cdot \Omega^{0.6}$ will be used (see Fig. 4).

B. Battery Model

An important component of an electric propulsion system is the battery pack. The battery often represents one of the heaviest components of the entire vehicle [38]. One of the most common types of batteries is the lithium polymer (LiPo), which offers a relatively high energy capacity along with low weight. Data of 240 LiPo batteries, produced by 11 different manufacturers,¹ are presented in Fig. 5. The figure shows the battery energy capacity E_B as a function of the battery mass m_B . The following representative relation between these two parameters is shown in Fig. 5:

$$E_B \text{ W} \cdot \text{h} = 4.04 \cdot (m_B \text{ kg})^2 + 139 \cdot m_B \text{ kg} + 0.0155 \quad (13)$$

III. Optimal Design of a Propulsion System

Any optimal design problem can be described mathematically as a search process for a design configuration that minimizes (or maximizes) a specific cost function that represents the design goal. This search process is usually carried out under certain design constraints.

Any design process requires an a priori definition of design variables, design constraints, and cost function. The design variables

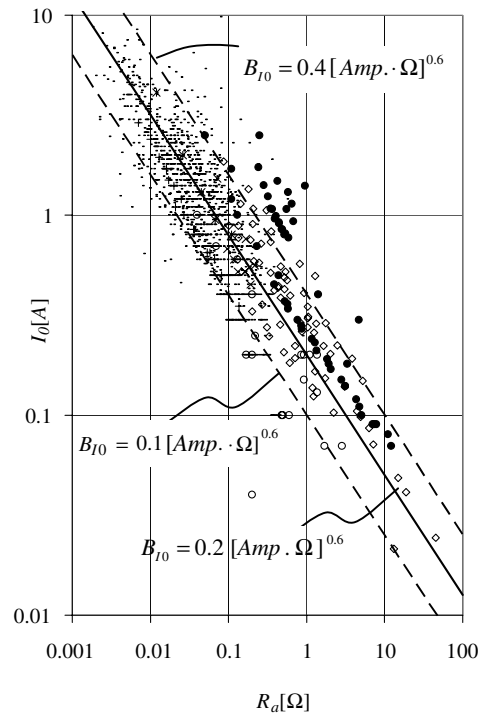


Fig. 4 No-load current as a function of internal resistance.

are parameters that are determined by the designer. In the general case of an electric propulsion system design, these variables are divided into five main categories: propeller general design variables, propeller blade design variables, blade cross-sectional design variables, electric motor design variables, and battery design variables.

The propeller's general design variables affect the global configuration of the propeller system and may include the following parameters: number of propellers, number of blades N_b , propeller radius R , and rotational speed Ω .

The blade's design variables are parameters that define the geometry and structure of each blade [namely, the distribution along the blade of the following parameters: pitch angle $\beta(r)$, chord $c(r)$,

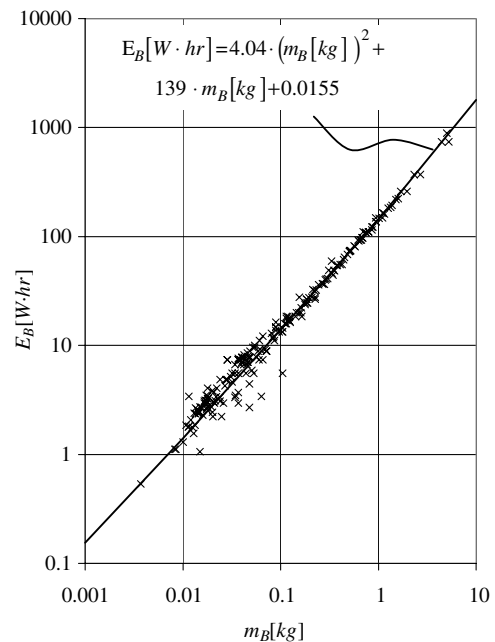


Fig. 5 Battery capacity as a function of battery mass.

¹Data available online at <http://www.flightpower.co.uk/>, <http://kokamamerica.com/news.htm>, <http://us.sanyo.com/Batteries>, and <http://www.thunderpowerrc.com/> [retrieved 15 March 2009].

sweep angle, dihedral angle (cone angle in the simplest case), mass and inertia, and structural properties].

The blade's cross-sectional design variables define the airfoil geometry as a function of a chordwise coordinate; thus, for example, [21] if the cross sections belong to the NACA-16 airfoil family [39], the geometry of each cross section is defined by two parameters (that may vary along the blade): thickness ratio $t/c(r)$ and design lift coefficient $C_{L-t}(r)$. In the current study, Clark-Y airfoils [40] are used, which are defined by the cross-sectional thickness ratio $t/c(r)$.

The electric system variables include the motor mass m_M and the battery-pack mass m_B .

The design constraints may include, for example, minimum or maximum chord size of the blade, allowable maximum stress, system mass, motor maximum mass, etc. The cost function is a quantitative measure of the success in achieving the design goal, and thus the cost function offers a measure of the quality of the design. A penalty method is used to solve the constrained optimization problem [41]. It leads to a new constrained cost function, which is minimized to find the optimal design, subject to all the constraints.

The present optimization scheme is based on a mixed-strategy approach that combines different optimization methods: 1) heuristic search using a simple genetic algorithm [42], 2) enumerative scheme using Nelder and Mead's [43] simplex scheme, and 3) derivative-based scheme using the steepest-descent method [44].

This approach ensures a thorough search for the global minimum by taking advantage of the strength of each of the preceding schemes. A detailed description of this strategy and examples of its application is presented in [21].

It should be emphasized that this design approach is by no means fully automatic. The designer plays a major role in the entire process. He or she follows the results during the design procedure and, based on these results, changes (if necessary) the optimization strategy. Thus, for example, in certain instances, the designer may decide to ease certain constraints to increase the flexibility of the search process or to freeze a few variables to avoid impractical results.

IV. Design of an Optimal Propulsion System for an Electric UAV

An electric mini UAV is considered. The mass of the vehicle without its propulsion system is $m_0 = 5.5$ kg. The wing area is $S_w = 0.72$ m², and the drag polar of the vehicle is described by the following equation:

$$C_D = 0.03 + 0.033 \cdot C_L^2 \quad (14)$$

where C_L and C_D are the vehicle's lift and drag coefficients, respectively.

A direct drive is used (the system does not include a gear box); namely, the rotational speed of the propeller is equal to that of the electric motor, Ω .

Because of operational constraints, the radius of the propeller is limited:

$$R \leq 0.15 \text{ m} \quad (15)$$

The blade tip Mach number M_{tip} is limited to subsonic speeds:

$$M_{\text{tip}} < 0.7 \quad (16)$$

As indicated previously, Clark-Y cross sections are used. The database for this airfoil family is limited to the following range of thickness ratios t/c [40]:

$$0.04 < \frac{t}{c} < 0.21 \quad (17)$$

For practical reasons, the chord is also limited:

$$c/R < 0.35 \quad (18)$$

The design variables of the current design problem are propeller radius R ; distribution of chord length along the blade, $c(r)$;

distribution of pitch angle along the blade, $\beta(r)$; distribution of thickness ratio along the blade, $t/c(r)$; mass of the electric motor, m_M ; and mass of the battery pack, m_B .

Note that the motor/propeller rotational speed does not appear as one of the design variables. The rotational speed is a result of a motor-propeller matching procedure. For specific flight condition (required thrust, airspeed, and atmospheric conditions) there is a certain rotational speed that makes the motor output power equal to the propeller-required power. This procedure is conducted for each analysis, and thus the rotational speed is part of the results.

The distribution of the various parameters along the blade is defined by their values at 11 radial stations; thus, there are 36 design variables in total. Although complex configurations of the blades (e.g., sweep and dihedral) may offer certain advantages [22,45], the present study is confined to two-bladed propellers with straight blades and zero cone angles.

In the present study, the electric motor mass and the battery-pack mass cannot exceed 5 and 20 kg, respectively:

$$m_M < 5 \text{ kg} \quad (19)$$

$$m_B < 20 \text{ kg} \quad (20)$$

The main task of the UAV is to loiter at low altitude above a certain area; thus, the design goal is an optimal propulsion system for loitering conditions that are defined by flight altitude (sea level in the present case) and airspeed V_l . In the present case,

$$V_l = 1.2 \cdot V_{\text{st}} \quad (21)$$

where V_{st} is the vehicle's stall airspeed. The stall airspeed is a function of the maximum lift coefficient $C_{L\text{max}}$:

$$V_{\text{st}}^2 = \frac{(m_0 + m_M + m_B) \cdot g}{\frac{1}{2} \cdot \rho_a \cdot S_w \cdot C_{L\text{max}}} \quad (22)$$

where g is the gravity acceleration, and the maximum lift coefficient is $C_{L\text{max}} = 1.4$.

Based on the vehicle's mass (which is a function of motor and battery mass), the stall and loitering airspeed are defined by using Eqs. (21) and (22). Then these flight conditions are used to calculate the required thrust based on the vehicle's drag polar [Eq. (14)].

According to Eq. (13) the battery energy capacity is a function of its mass. It is assumed in the present study that 70% of the total energy capacity is used for loitering and that the other 30% are used for other flight phases (takeoff, climb, landing, etc.), payload requirements, and vehicle's subsystems.

A. Single-Goal Design

As indicated previously, the main task of the UAV is loitering. Thus, a main design goal is to optimize loitering: namely, to maximize loiter time. On the other hand, because the vehicle is designed for tactical field operation, rate of climb after takeoff represents a very critical parameter that is related to vehicle survivability as well as the safety of nearby people. Thus, two different design goals are defined: maximum loiter time t_l and maximum rate of climb (ROC) at loitering speed. As a first stage in this study, each of these goals will be dealt with separately as a single-goal design. For maximum loiter time, the cost function (to be minimized) is $-t_l$ (where $-t_l$ is the minus of loiter time). Similarly, for maximum rate of climb, the cost function is $-\text{ROC}$ (minus of ROC).

Figure 6 presents the optimal blade design for these two different cost functions. The figure presents the distribution of pitch angle β , thickness t , and chord c along the blade. The geometric characteristics of the two propellers are different: the pitch angle, chord length, and cross-sectional thickness of the maximum-ROC design are larger than the same parameters in the case of maximum-loiter-time design. This increase represents an effort to obtain maximum thrust in the case of maximum-ROC design (the propeller rotational speed is limited because of the tip-speed constraint).

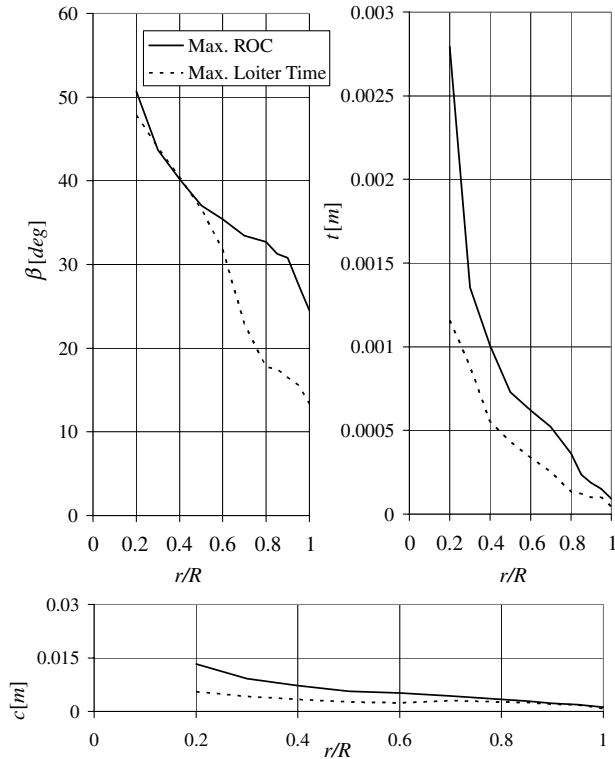


Fig. 6 Single-goal design: geometry of maximum loiter time and maximum-rate-of-climb propellers.

Important differences between the two optimal designs are evident from Table 1. The maximum-ROC propulsion system has zero battery mass, because maximum thrust is required in this case, but there is no requirement for a finite flight time. On the other hand, the maximum-loiter-time design requires high energy capacity; thus, the mass of the battery increases significantly, but the vehicle's ROC at loiter is zero, which presents an impractical flight condition. Thus, these two single-goal optimal designs are impractical, yet they are important because they present the boundaries of practical designs and they offer important insight into design trends.

It should be noted (Table 1) that because the total masses of the two designs are different, there are significant differences in loiter speed between both cases [see Eqs. (21) and (22)]. The battery of the maximum-loiter-time design does not reach the limit of 20 kg, because at a certain point, an increase of the battery mass results in an

increase in loiter speed and, consequently, an increase in vehicle's drag that offsets the beneficial effect of increasing the energy capacity.

Table 1 also presents the rotational speed Ω , motor output power P_{out} , propeller thrust T , and efficiencies of the propeller and the electric system, η_P and η_S , respectively. For each optimal design, these parameters are given for two flight conditions: loiter and maximum ROC.

The propeller's efficiency is defined as follows:

$$\eta_P = \frac{T \cdot V_F}{P_{out}} \quad (23)$$

It is interesting to note in Table 1 that for the maximum-loiter-time design, the flight conditions of loiter and maximum ROC are identical: At loiter the constraint on the maximum blade tip speed, Eq. (16), is active and does not allow any increase in power, thus resulting in zero ROC. On the other hand, for the design of maximum ROC, there are differences between the two flight conditions. Although loitering is carried out at $P_{out} = 116$ W, maximum ROC is obtained for $P_{out} = 1000$ W, where the constraint of maximum blade tip speed becomes active again.

The efficiency of the propeller for maximum ROC is relatively low at that flight condition. Ideal propeller efficiency $\eta_{P-ideal}$ is defined as the efficiency under the following ideal conditions [46]: 1) zero wake rotation, 2) zero cross-sectional friction drag ($C_d = 0$), and 3) uniform axial induced velocity.

The relation between the ideal propeller efficiency $\eta_{P-ideal}$ and the ideal propeller-required power (motor output power) P_{out} becomes [46]

$$P_{out} = 2 \cdot \rho_a \cdot V_F^3 \cdot \pi \cdot R^2 \cdot \frac{1 - \eta_{P-ideal}}{\eta_{P-ideal}^3} \quad (24)$$

For the present case of $P_{out} = 1000$ W and $V_F = 15.1$ m/s, the ideal efficiency according to Eq. (24) is $\eta_{P-ideal} = 0.612$ (compared with a nonideal value of $\eta_P = 0.561$). This indicates that if the power of the propeller is increased (to increase ROC in this case) and the radius is limited, efficiency may decrease significantly.

The rotational speeds of the two designs are different at loitering. This difference is due to the difference in the loitering airspeed V_l , a difference that is a result of the various vehicles' total mass m_{total} [see Eqs. (21) and (22)].

Note that both designs have a radius of 0.15 m, the maximum allowed value. This trend continued along the entire present study, and thus data about the propeller radius are not repeated in what follows.

B. Dual-Goal Design

A practical design presents a compromise between the two extreme and impractical design goals of Sec. IV.A. This case of dual-goal design leads to a multi-objective optimization problem. In this case, a Pareto front of the cost function can be drawn. This Pareto front is obtained by defining maximum loiter time as the goal, under specific ROC constraints. The two designs of Fig. 6 represent the extreme right and left points of the Pareto front, which is shown in Fig. 7. This figure also presents the mass breakdown. As indicated previously (Table 1), battery mass is high for long endurance and low ROC, whereas for short endurance and high ROC, battery mass decreases significantly and the motor mass reaches its maximum value. The limit of the motor mass (5 kg) is reached for ROC = 2 m/s, and for larger values of ROC, the motor mass remains unchanged. As indicated previously, the battery mass does not reach its limit (20 kg) and only gets close to it for the maximum endurance design. Still, the battery mass exceeds the basic vehicle mass m_0 for ROC close to 3.5 m/s, which means that for most of the range of ROC, the battery mass represents a significant portion of the total vehicle mass.

Figure 8 presents the propeller's efficiency at the maximum-ROC operating conditions. The ideal efficiency according to Eq. (24) is

Table 1 Single-goal design results for maximum-loiter-time and maximum-rate-of-climb designs

Parameter	Design for maximum loiter time	Design for maximum ROC
t_l , s	17,175	0
ROC, m/s	0	4.876
m_M , kg	2.52	5.0
m_B , kg	19.4	0.0
m_{total} , kg	26.9	10.0
V_F , m/s	24.8	15.1
<i>Operation at loiter</i>		
Ω , rpm	15,160	6780
P_{out} , W	505	116
T , N	16.6	6.2
η_P	0.815	0.808
η_S	0.818	0.792
<i>Operation at maximum ROC</i>		
Ω , rpm	15,160	15,160
P_{out} , W	505	1000
T , N	16.6	37.1
η_P	0.815	0.561
η_S	0.818	0.738

also shown. The actual efficiency is lower than the ideal value by approximately 0.06.

C. Dual-Goal Design Under Mass and Structural Constraints

To make the design more practical, the total mass of the vehicle is limited to 8 kg. This limit is based on a typical weight that can be carried by a single soldier:

$$m_{total} \leq 8 \text{ kg} \tag{25}$$

This means that the total mass of the propulsion system (motor and battery pack) cannot exceed 3 kg.

Table 2 and Fig. 9 present the data and geometry of the two single-goal designs: maximum ROC and maximum loiter time under a total mass constraint (without additional constraints).

In general, cross-sectional pitch angles of the maximum-loiter-time design are higher than the maximum-ROC design. This reflects the difference in rotational speed. The two designs have to produce the same thrust at loiter (the total vehicle mass is the same); thus, because the rotational speed of the maximum-loiter-time design is

Table 2 Single-goal design under total mass constraint-Results for maximum-loiter-time and maximum-rate-of-climb designs

Parameter	Design for maximum loiter time	Design for maximum ROC
t_l, s	9750	0
ROC, m/s	0	3.63
m_M, kg	0.41	3.0
m_B, kg	2.59	0.0
m_{total}, kg	8.0	8.0
$V_F, m/s$	13.5	13.5
<i>Operation at loiter</i>		
Ω, rpm	9700	7360
P_{out}, W	81.5	82.5
T, N	4.94	4.94
η_P	0.820	0.810
η_S	0.812	0.820
<i>Operation at maximum ROC</i>		
Ω, rpm	9700	15,150
P_{out}, W	81.5	600
T, N	4.94	25.9
η_P	0.820	0.584
η_S	0.812	0.802

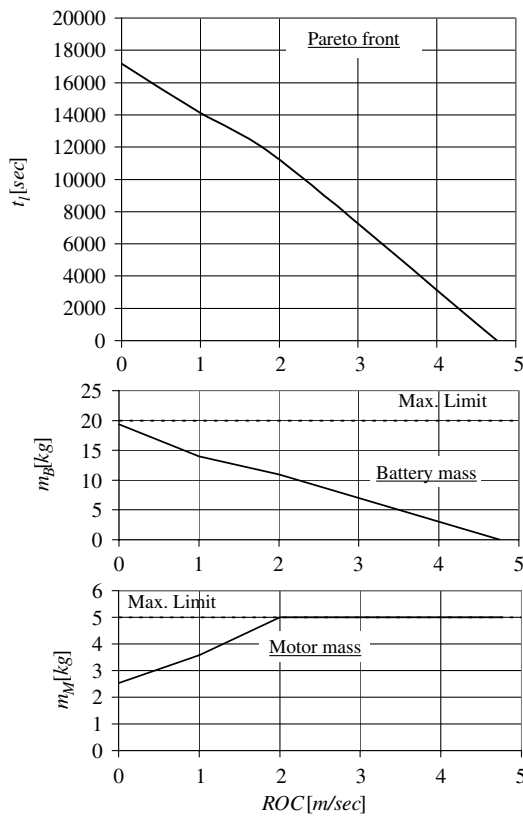


Fig. 7 Dual-goal design: Pareto front and mass breakdown.

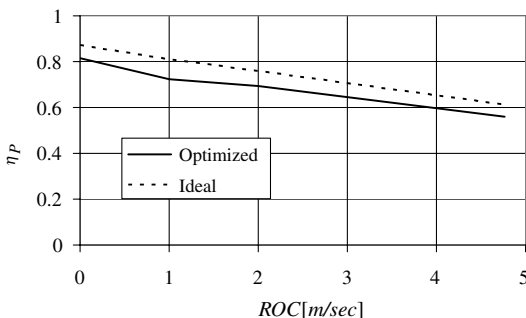


Fig. 8 Dual-goal design: maximum propeller's efficiency at various ROC values.

lower than that of the maximum-ROC design, the pitch angle of the first one increases.

One of the characteristics of the optimal designs in Fig. 9 is their very small chord and thickness at the outer cross sections of the blades. Such designs may not comply with structural requirements [21]; thus, structural constraints should also be considered.

It is assumed that the blade is made of aluminum 7075-T6. The yield stress of this material is 5.03×10^8 Pa. The maximum von Mises stress $\bar{\sigma}$ will be limited to

$$\bar{\sigma} < 1.5 \times 10^8 \text{ Pa} \tag{26}$$

The stress constraint is calculated for the maximum-ROC conditions, which represent an extreme flight condition from the point of view of loads that act on the blades.

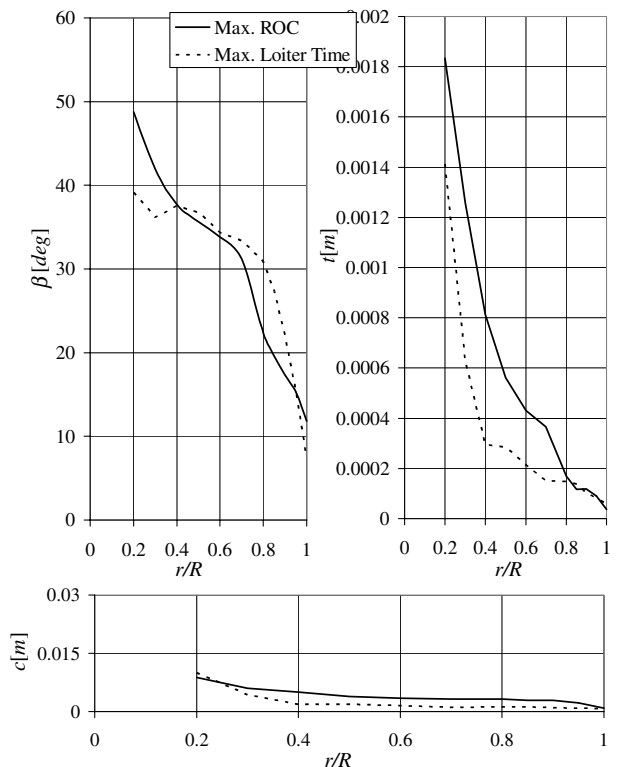


Fig. 9 Single-goal design under total mass constraint: propeller designs for maximum loiter time and maximum rate of climb.

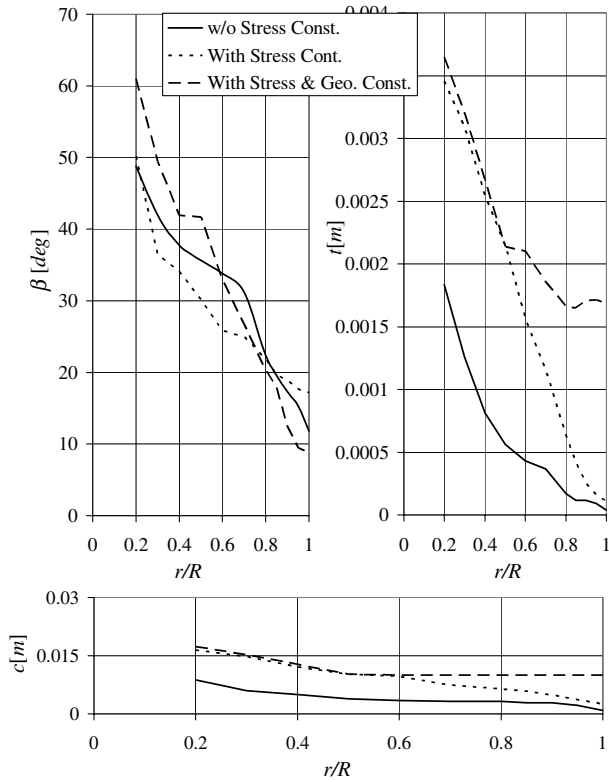


Fig. 10 Maximum-ROC design under total mass constraint: influence of structural and geometric constraints.

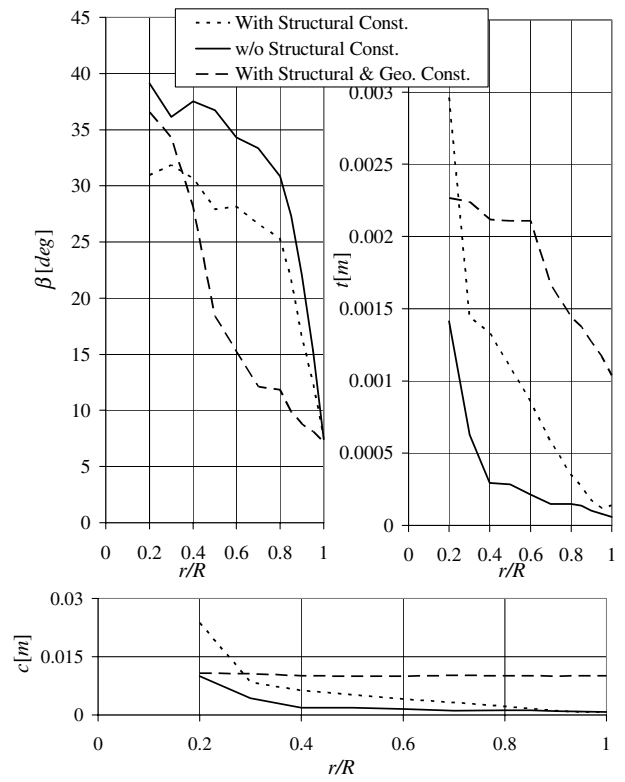


Fig. 11 Maximum-loiter-time design under total mass constraint: influence of additional constraints.

Figures 10 and 11 present comparisons between optimal designs with and without structural constraints for maximum ROC and maximum loiter time, respectively. The application of structural constraints significantly increases the chord lengths and thicknesses of the blades.

After the application of the structural constraints, the chord length of the optimized blades is still small: less than 3 mm at the outer 30% of the blades' length for the maximum-loiter-time design and less than 5 mm at the outer 15% portion of the maximum-ROC design. Although the two designs comply with the structural constraints (26), the blade geometry is impractical and will not comply with maintenance and operational constraints. Thus, additional geometric constraints limiting the minimum blade chord are introduced:

$$c \geq 0.01 \text{ m} \quad (27)$$

Figures 10 and 11 also present the geometry of optimal blades under combined structural [Eq. (26)] and geometric [Eq. (27)] constraints. Tables 3 and 4 present the characteristics of these two designs under the various constraints. Note that the introduction of structural constraints leads to a significant reduction of rotational speed of both designs, to keep stresses within their limit. Adding geometric constraints decreases the rotational speed even further: wider and thicker blades result in larger centrifugal forces, and thus a further reduction of the rotational speed is needed. The decrease of the rotational speed results in a decrease of the available thrust at maximum ROC (for the optimal design of that flight condition) and thus a reduced ROC. In the case of maximum-loiter-time design, the reduction in rotational speed is accompanied by a reduction in the efficiencies of the propeller and electric system. This leads to a reduction in loiter time.

Table 3 Maximum-ROC design under total mass constraint: influence of additional constraints

Parameter	Without additional constraints.	With structural constraints	With structural and geometric constraints
t_l , s	0	0	0
ROC, m/s	3.61	3.54	3.45
m_M , kg	3.00	3.00	3.00
m_B , kg	0.00	0.00	0.00
m_{total} , kg	8.0	8.0	8.0
V_F , m/s	13.5	13.5	13.5
<i>Operation at loiter</i>			
Ω , rpm	7360	5780	4961
P_{out} , W	82.5	84.4	86.5
T , N	4.94	4.94	4.94
η_P	0.810	0.791	0.773
η_S	0.820	0.784	0.748
<i>Operation at maximum ROC</i>			
Ω , rpm	15,150	11,320	9660
P_{out} , W	600	600	600
T , N	25.9	25.4	24.9
η_P	0.584	0.574	0.562
η_S	0.802	0.723	0.668

Table 4 Maximum-loiter-time design with total mass constraint: influence of additional constraints

Parameter	Without additional constraints	With structural constraints	With structural and geometric constraints
t_l , s	9750	9340	8900
ROC, m/s	0	0	0
m_M , kg	0.41	0.42	0.43
m_B , kg	2.59	2.58	2.57
m_{total} , kg	8.0	8.0	8.0
V_F , m/s	13.5	13.5	13.5
<i>Operation at loiter</i>			
Ω , rpm	9700	7800	6890
P_{out} , W	81.5	83.8	86.1
T , N	4.94	4.94	4.94
η_P	0.820	0.797	0.775
η_S	0.812	0.804	0.792
<i>Operation at maximum ROC</i>			
Ω , rpm	9700	7800	9660
P_{out} , W	81.5	83.8	86.1
T , N	4.94	4.94	4.94
η_P	0.820	0.797	0.775
η_S	0.812	0.804	0.792

Figure 12 presents the Pareto front and mass breakdown of the dual design case under a total mass constraint and various combinations of other constraints. Naturally, and similar to the results that were shown in Fig. 7, as the ROC increases, the loiter time decreases. The influence of adding structural constraints is a reduction of about 5% of loiter time, with a negligible influence on the mass breakdown. The influence of adding geometric constraints is an additional 5% reduction of loiter time and still a negligible influence on the mass breakdown.

According to Fig. 12, loiter time and mass breakdown of the three designs are very similar; thus, it can be concluded that the addition of structural and geometric constraints results in only a relatively small reduction of loiter time.

The last conclusion can be explained by examining the axial induced velocity W_a and the spanwise loading distribution dT/dr of the different optimal designs under the various constraints. Figure 13

presents comparisons between the maximum-ROC designs. It is shown that the induced velocity and spanwise aerodynamic loading distributions are very similar in all cases. As a result of applying structural constraints, the maximum of the loading gets closer to the blade root to reduce the bending moment at the root. Adding geometric constraints result in stronger blades, and thus the maximum of the aerodynamic loading occurs closer to the blade's tip. Similar trends as a result of adding various constraints also appear in the case of maximum-loiter-time designs.

V. Sensitivity Study

The electric motor model includes four parameters: B_{P-M} is the maximum power-to-mass ratio, B_{Kv} is the speed-constant parameter, B_{Ra} is the internal-resistance parameter, and B_{J0} is the no-load

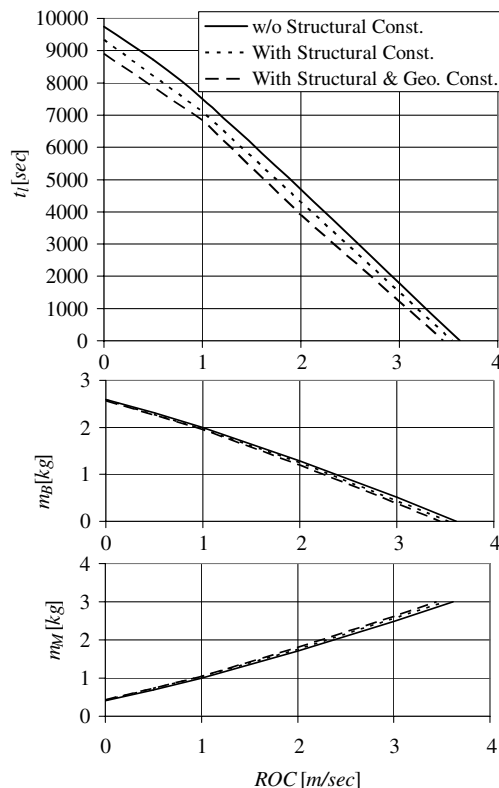


Fig. 12 Influence of additional constraints on a dual-goal design with total mass constraint; Pareto front and mass breakdown.

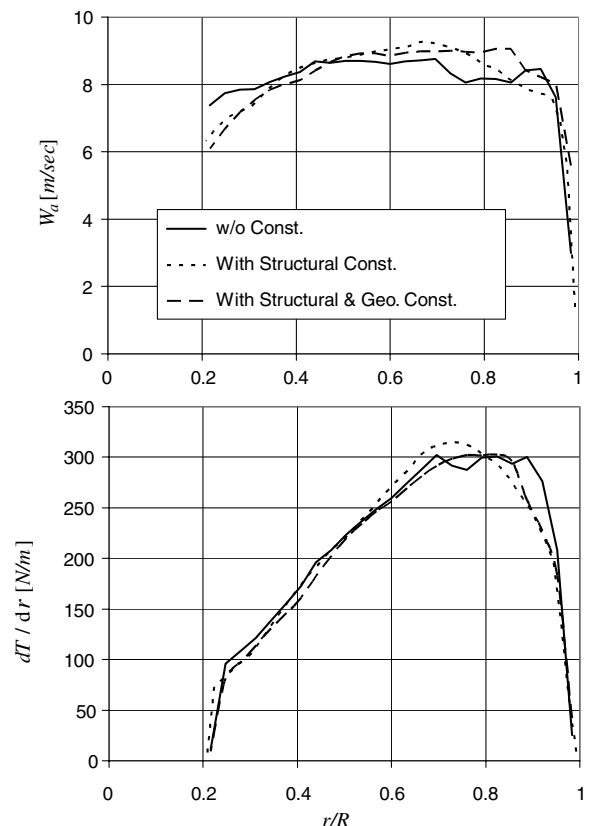


Fig. 13 Maximum-ROC designs: spanwise induced velocity and loading distributions.

current parameter. The battery is defined by the ratio between its energy capacity and mass: the energy density B_{EB} .

During the study of the previous section, nominal representative values of all these parameters were used. Yet it was shown that there are significant differences between various motors. The purpose of the present section is to study the influence of these differences on the design and performance of the optimal propulsion system. The study will include variations of one of the parameters, whereas all the other parameters are constant and equal to their nominal values.

The design goal during this study is to maximize loiter time while requiring minimal ROC of 2 m/s under the structural and geometric constraints of the previous section [Eqs. (25–27)].

A. Maximum Power-to-Mass Ratio B_{P-M}

The first parameter to be investigated is the maximum power-to-mass ratio B_{P-M} . This parameter has been varied between its limit values, as defined by Eq. (2). The results are presented in Fig. 14, in which loiter time t_l , motor mass m_M , and battery mass m_B are presented as functions of B_{P-M} . As expected, as B_{P-M} increases, loiter time increases too, because a reduction of the motor mass allows an increase of the battery mass. As B_{P-M} increases, the rate of increase of loiter time with B_{P-M} decreases. This is due to the fact that as the motor mass decreases, a large relative changes of the motor mass results in only a very small relative increase of the battery mass.

Because increase in B_{P-M} means, in many cases, a reduction in reliability (aeromodel motors), the designer has to decide when the increase in loiter time due to B_{P-M} increase is not worth the accompanied decrease in reliability.

B. Motor Speed-Constant Parameter B_{Kv}

Another parameter that defines the electric motor characteristics is the motor speed-constant parameter [see Eq. (7)]. Although the

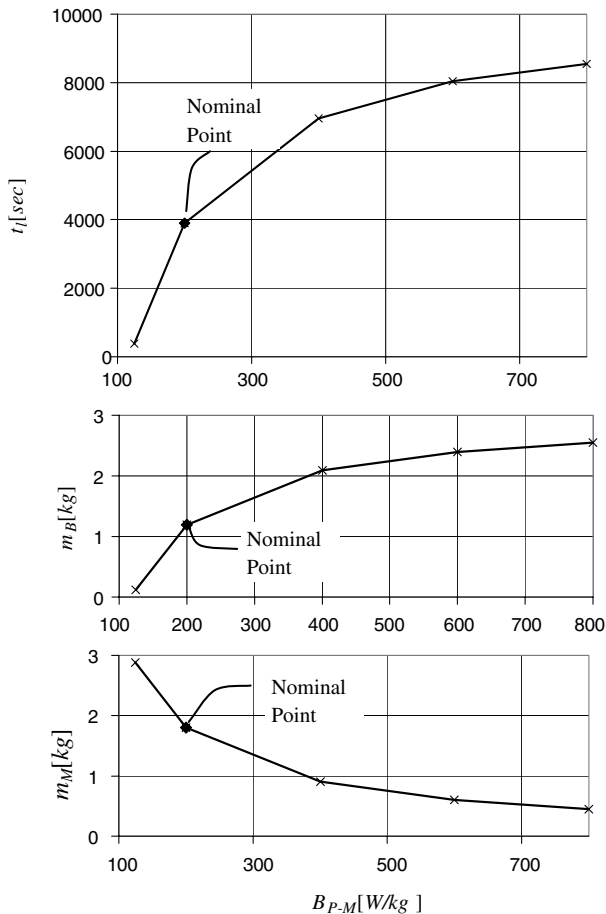


Fig. 14 Loiter time and mass breakdown as functions of maximum power-to-mass ratio B_{P-M} ; maximum endurance with ROC = 2 m/s.

nominal value of this parameter in the previous examples was $B_{Kv} = 170 \text{ rpm} \cdot \text{kg/V}$, according to Eq. (8), its value may vary significantly.

Figure 15 presents loiter time and mass breakdown as functions of the speed-constant parameter. The variations of the mass breakdown are negligible and loiter time varies by only 4% along the entire range. The influence of the motor speed-constant parameter on the optimal blade design is also negligible, whereas the main influence is on the rotational speed. Figure 16 presents the rotational speed of the propeller at two flight conditions: loiter and ROC = 2 m/s. In both cases, as B_{Kv} increases, the rotational speed increases too. Still, the variations do not exceed 10% along the entire range of B_{Kv} .

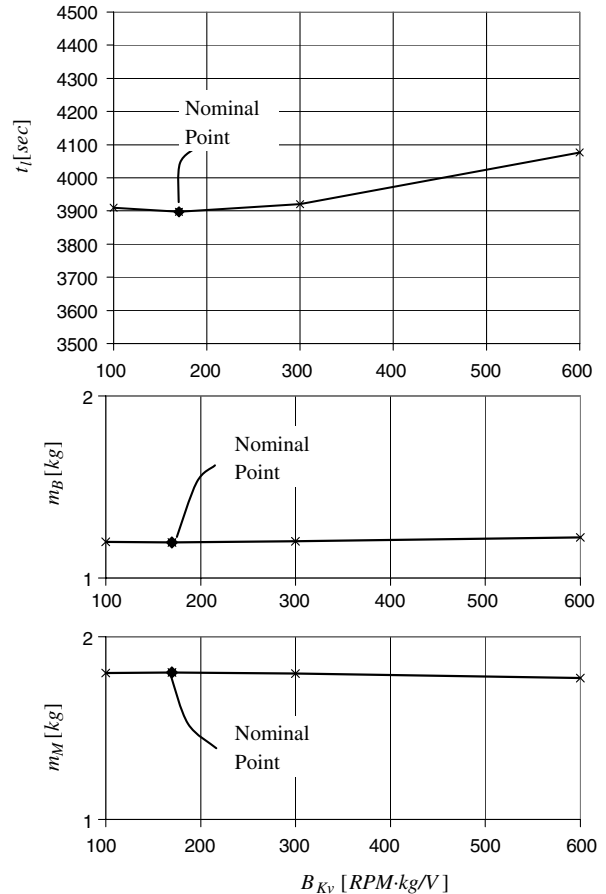


Fig. 15 Loiter time and mass breakdown as functions of motor speed-constant parameter B_{Kv} ; maximum endurance with ROC = 2 m/s.

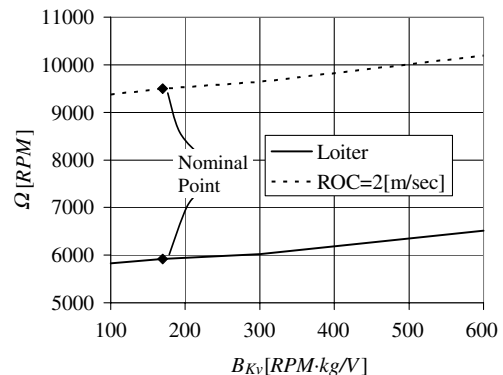


Fig. 16 Propeller rotational speeds at loiter and ROC = 2 m/s as functions of motor speed-constant parameter B_{Kv} .

C. Internal-Resistance Parameter B_{Ra}

The internal-resistance parameter B_{Ra} is defined by Eq. (9). Figure 17 presents loiter time and optimal mass breakdown as functions of the internal-resistance parameter. According to this figure, there is an optimal value of this parameter, which is $12,000 \text{ V}^2 \cdot \Omega/\text{rpm}^2$ and gives a maximum loiter time of 4220 s. Figure 18 presents the influence of B_{Ra} on the internal resistance R_a , no-load current I_0 , and electric system efficiency η_E (for both flight conditions: loiter and climbing). As B_{Ra} increases, the internal resistance decreases and the no-load current increases. According to Eq. (5), the efficiency of the motor increases as R_a and I_0 decrease, and vice versa. Thus, as B_{Ra} increases, the opposite trends of R_a and I_0 result in a point of maximum efficiency, leading to a maximum value of loiter time, as indicated previously.

For a wide range of internal-resistance parameter,

$$2500 \text{ V}^2 \cdot \Omega/\text{rpm}^2 < B_{Ra} < 100,000 \text{ V}^2 \cdot \Omega/\text{rpm}^2$$

the total variation of the loiter time is 15%, which indicates the small influence of this parameter over the optimal system characteristics. This is true also for the mass breakdown.

D. No-Load Current Parameter B_{I_0}

Figure 19 presents loiter time and optimal mass breakdown as functions of the no-load current parameter B_{I_0} that was defined by Eq. (11). The influence of this parameter on the optimal mass breakdown is negligible, whereas it results in variations of less than 10% in loiter time. Figure 20 presents the influence of B_{I_0} on internal resistance R_a , no-load current I_0 , and electric system efficiency (at loiter and climbing). It is shown that the internal resistance is not

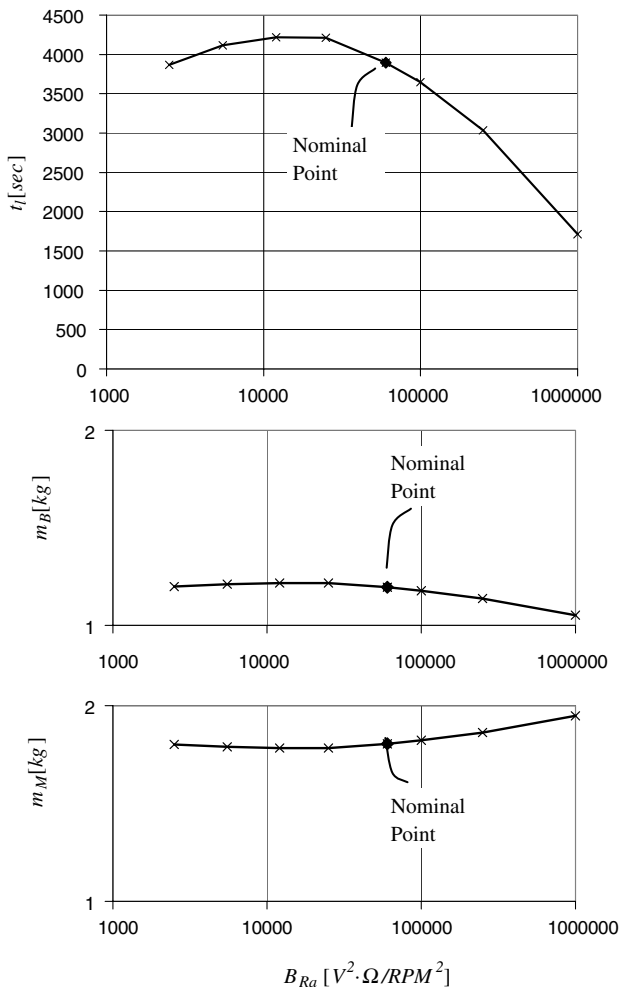


Fig. 17 Loiter time and mass breakdown as functions of internal-resistance parameter B_{Ra} ; maximum endurance with ROC = 2 m/s.

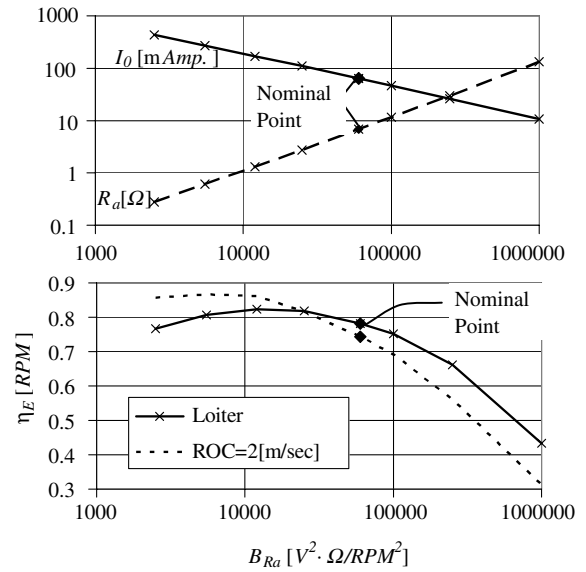


Fig. 18 No-load current, internal resistance, and electric system efficiency at loiter and ROC = 2 m/s as functions of internal-resistance parameter B_{Ra} .

affected by variations of the no-load current parameter. On the other hand, the no-load current increases as a result of increasing B_{I_0} . Thus, according to Eq. (5), as B_{I_0} increases, the system efficiency decreases and loiter time decreases as well.

E. Battery Energy Density B_{EB}

The model of LiPo batteries is given by Eq. (13). This model exhibits a very good agreement with existing batteries (see Fig. 5)

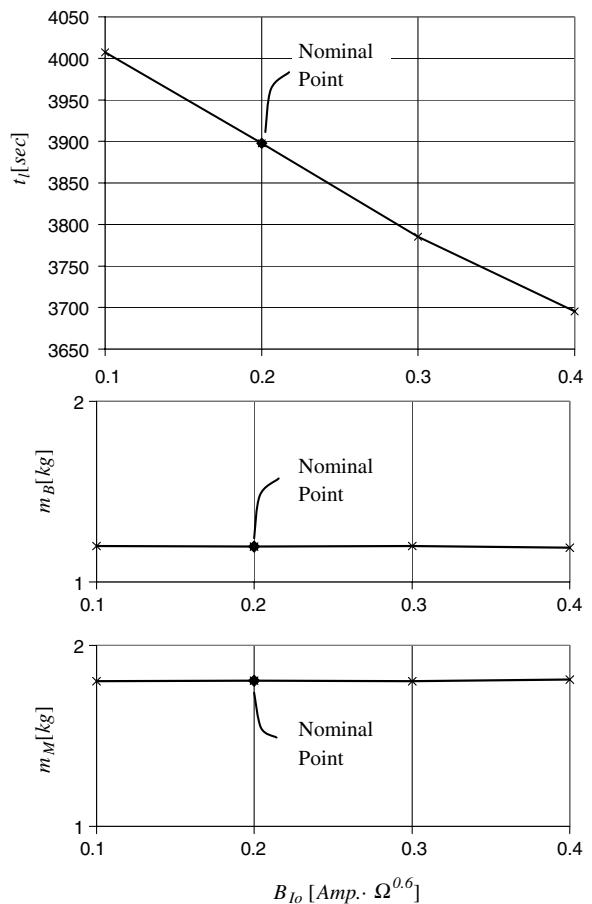


Fig. 19 Loiter time and mass breakdown as functions of no-load current parameter B_{I_0} ; maximum endurance with ROC = 2 m/s.

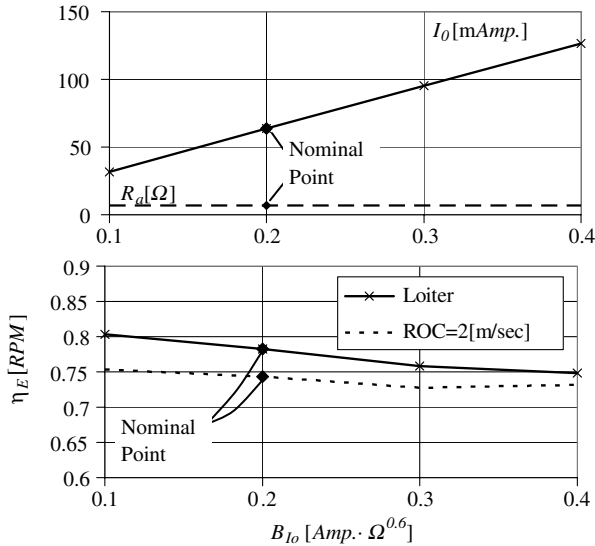


Fig. 20 No-load current, internal resistance, and electric system efficiency at loiter and $ROC = 2$ m/s as functions of internal-resistance parameter B_{Ra} .

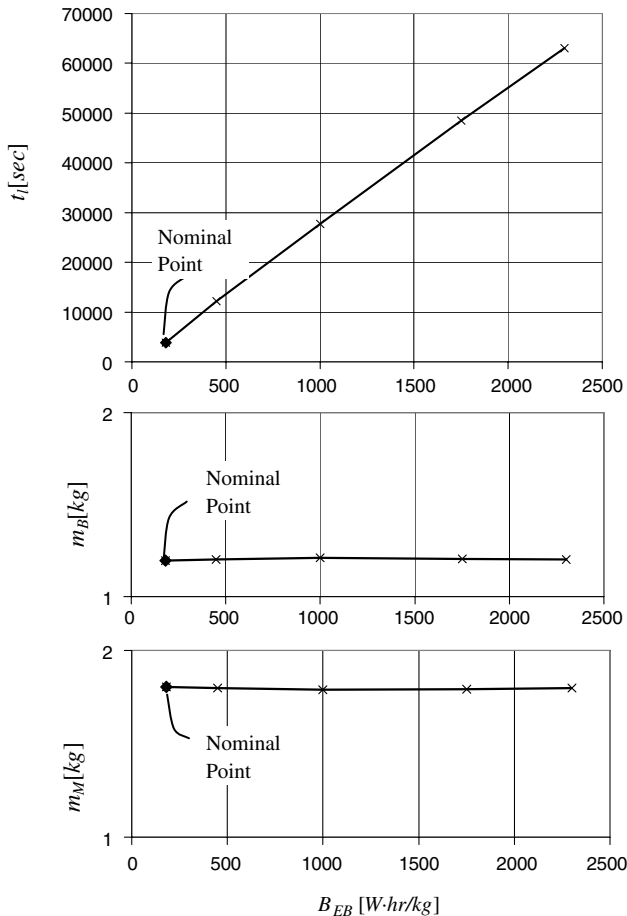


Fig. 21 Loiter time and mass breakdown as functions of battery energy density B_{EB} ; maximum endurance with $ROC = 2$ m/s.

with relatively small scatter. For the present sensitivity study, a linear model of variations about the nominal case is used:

$$E_B \cdot W \cdot h = B_{EB} \cdot m_B \text{ kg} \quad (28)$$

where B_{EB} is the battery energy density (the energy per unit mass). A value of $B_{EB} = 180$ W · h/kg exhibits a good agreement with the

curve of Fig. 5. During the years, there has been a continuous, although fairly slow, improvement in the energy density of electrochemical batteries [23]. In the future, regenerative fuel cells may offer a major improvement of energy density above 400 W · h/kg [47] and up to 2300 W · h/kg [48].

Figure 21 presents loiter time and optimal mass breakdown as functions of the energy density. It is shown that the mass breakdown is practically unaffected by variations of the energy density, whereas loiter time increases linearly with B_{EB} . The optimal blades design also is not affected by variations of the energy density of the battery.

VI. Conclusions

A comprehensive method for optimal design of electric propulsion systems for UAVs has been presented. The method is based on an MDO approach that includes aerodynamic, structural, electric, and performance analysis tools. These analysis tools are combined with three different optimization schemes to obtain the optimal design according to various design goals, using various design variables, and under various constraints.

Although the aerodynamic and structural models of the propeller were presented elsewhere, the derivation of the electric motor model was presented in detail. This is a simplified model that is suitable for optimization: a large number of analyses are carried out, and thus a numerically efficient model is required. This model includes four parameters that are defined based on examining a vast motor data from various manufacturers. A model of the energy capacity of the battery pack as a function of its mass is derived in a similar manner.

The new design tool was applied to design a propulsion system for an electric mini UAV. The design includes the propeller, motor, and battery. There are two important performance indicators for this vehicle: loiter time, which is related directly to its main reconnaissance task and should be maximized, and rate of climb, which is directly related to the survivability and safety of the vehicle. The study starts with single-goal optimal designs of a propeller for maximum loiter time (which yields zero rate of climb because of propeller constraints) and a propeller for maximum rate of climb (which yields zero loiter time due to zero battery mass). The optimization is carried out with certain upper limits on the motor and battery masses. Although these two designs are impractical, they are important because they give an insight into the two extreme design trends. Thus, for example, because the propeller radius is limited, maximum rate of climb results in relatively low propeller efficiencies. To obtain the high thrust that is necessary for high rate of climb, the chord in this design is roughly twice as large as the chord of the propeller design for maximum loiter time.

More practical designs lie between the two extreme impractical cases. These designs are shown by a Pareto front, representing propellers that yield maximum loiter time for changing rate of climb capabilities. As the required rate of climb increases, the engine mass increases and loiter time decreases. It is interesting to note the complex influence of motor and battery mass: increase in motor mass improves rate of climb, and increase in battery mass extends loiter time. Yet increasing vehicle mass results in higher loiter and climb airspeeds, thus making these flight conditions less efficient.

If the battery and motor masses are not limited, the total vehicle mass becomes too large to be carried by a soldier, which is a common requirement from such tactical systems (mini UAVs). Thus, it becomes important to use comprehensive tools, such as the present one, that allow the introduction of additional constraints such as an upper limit on the total mass of the UAV.

The optimal designs that are obtained based on aerodynamic/performance considerations result in very narrow and thin blades that are impractical when structural and maintenance aspects are considered. Thus, structural constraints that impose upper limits on the stresses are added. Yet, even under structural constraints, the blades are still too thin and narrow. Thus, geometric constraints that pose lower limits on the chord length are also added. It is interesting to note that in spite of the significant increase in the size of the blades' cross sections due to the introduction of these constraints, the design trends are unchanged. In addition, the design goals (namely, loiter

time under minimum rate of climb constraint) are usually reduced by no more than 10%.

The introduction of structural and geometric constraints results in a significant reduction of the propeller rotational speed. Consequently, the tension stresses due to centrifugal forces do not exceed the allowed levels. Moreover, the MDO process is also capable of reducing the bending moment at the root due to aerodynamic loads by moving the point of maximum loading toward the blade root.

There are differences in the characteristics of electric components between different manufacturers and different technologies and for other reasons. A sensitivity study was carried out to study the influence of such variations on the optimal system design. This paper presents the influence of variations of four motor parameters: maximum power-to-motor-mass ratio, motor speed-constant parameter, internal-resistance parameter, and zero-load current parameter. In addition, the sensitivity to the battery energy density is also examined.

Increasing the maximum power-to-motor-mass ratio results in a beneficial effect of increasing loiter time. Yet the rate of increase of loiter time reduces as the motor mass decreases. Because a reduction of this parameter is accompanied, in many cases, by a parallel reduction of the motor's reliability and availability, at a certain stage, a further increase of the maximum power-to-motor-mass ratio is worthless.

Variations of the motor speed parameter exhibit negligible effect on the mass breakdown. Loiter time changes by less than 5% for the entire range of variations. The propeller rotational speed exhibits a somewhat larger change, resulting in only small changes of the optimal blades design.

There is an optimal value of the internal-resistance parameter that maximizes the loiter time. Still, the relative variation in loiter time and mass breakdown are small. This is also true for the no-load current parameter, which has a small influence on the system characteristics. Increase of the battery energy density increases loiter time in a linear manner. Nevertheless, this change does not affect the mass breakdown.

It can be concluded, based on the sensitivity study, that the battery density and maximum power-to-mass ratio have the largest influences on the design and performance of the system. The other parameters have a relatively minor influence on the vehicle performance, but they may influence the optimal design. The present study shows once more that when optimizing a propeller-based propulsion system, it is essential to simultaneously consider all the components of this system: propeller, motor, and energy source, as well as the vehicle's characteristics.

Acknowledgments

This research was supported by the Bernard M. Gordon Center for Systems Engineering at Technion—Israel Institute of Technology. The authors would like to thank the center for this support. The authors would also like to thank Raul Rabinovici from Ben-Gurion University and Vladimir Grinberg from Bental Motion Systems for their assistance with the development of the electric system model.

References

- [1] "Unmanned Aerial Vehicles Roadmap 2000–2025," http://www.globalsecurity.org/intell/library/reports/2001/uavr0401.htm#_Toc509906768 [retrieved 15 Mar. 2009].
- [2] Ott, J., and Biezd, D., "Design of a Tube-Launched UAV," AIAA 3rd "Unmanned Unlimited" Technical Conference, Workshop and Exhibit, AIAA Paper 2004-6493, Chicago, 20–23 Sept. 2004.
- [3] Nagel, A., Levy, D. E., and Shepshelovich, M., "Conceptual Aerodynamic Evolution of Mini/Micro UAV," 44th AIAA Aerospace Sciences Meeting and Exhibit, AIAA Paper 2006-1261, Reno, NV, 9–12 Jan. 2006.
- [4] Keennon, M. T., and Grasmeyer, J. M., "Development of the Black Widow and Microbat MAVs and a Vision of the Future of MAV Design," AIAA/ICAS International Air and Space Symposium and Exposition: The Next 100Y, AIAA Paper 2003-2901, 14–7 July 2003.
- [5] Betz, A., "Schraubenpropeller mit Geringstem Energieverlust," *Königliche Gesellschaft der Wissenschaften* Vol. 2, 1919, pp. 193–217; also "Screw Propeller with Minimum Energy Loss," Technical Translation 736, translated by D. A. Sinclair, National Research Council Library, Ottawa, Canada, 1958.
- [6] Adkins, C. N., and Liebeck, R. H., "Design of Optimum Propellers," *Journal of Propulsion and Power*, Vol. 10, No. 5, Sept.–Sept. 1994, pp. 676–682. doi:10.2514/3.23779
- [7] Roncz, G. J., "Propeller Development for the Rutan Voyager," General Aviation Aircraft Meeting and Exposition, Society of Automotive Engineers, Paper SAE-891034, Wichita, KS, 11–13 Apr. 1989.
- [8] Succi, G. P., "Design of Quiet Efficient Propellers," SAE Business Aircraft Meeting, Society of Automotive Engineers Paper 790584, Apr. 1979.
- [9] Patrick, H., Finn, W. R., and Stich, K. C., "Two and Three-Bladed Propeller Design for the Reduction of Radiated Noise," 3rd AIAA/CEAS Aeroacoustics Conference, AIAA Paper 97-1710-CP, Atlanta, GA, 12–14 May, 1997.
- [10] "White Paper on Current State of the Art," AIAA Technical Committee on Multidisciplinary Design Optimization (MDO), Jan. 1991, http://endo.sandia.gov/AIAA_MDOTC/sponsored/aiaa_paper.html [retrieved 15 Mar. 2009].
- [11] Sobieszcanski-Sobieski, J., and Haftka, R. T., "Multidisciplinary Aerospace Design Optimization: Survey of Recent Development," *Structural optimization*, Vol. 14, No. 1, 1997, pp. 1–23. doi:10.1007/BF01197554
- [12] Bennet, R. L., "Application of Optimization Methods to Rotor Design Problems," *Vertica*, Vol. 7, No. 3, 1983, pp. 201–208.
- [13] Friedmann, P., "Application of Modern Structural Optimization to Vibration Reduction in Rotorcraft," *Vertica*, Vol. 9, No. 4, 1985, pp. 363–376.
- [14] Ormsbee, A. I., and Woan, C. J., "Optimum Acoustic Design of Free Running Low Speed Propellers," AIAA Aircraft Systems & Technology Meeting, AIAA Paper 77-1248, Seattle, WA, 22–24 Aug. 1977.
- [15] Chang, L. K., and Sullivan, J. P., "Optimization of Propeller Blade Shape by an Analytical Method," AIAA/SAE/ASME 18th Joint Propulsion Conference, AIAA Paper 82-1125, Cleveland, OH 21–23 June, 1982.
- [16] Chang, L. K., and Sullivan, J. P., "Optimization of Propeller Blade Twist by an Analytical Method," *AIAA Journal*, Vol. 22, No. 2, Feb. 1984, pp. 252–255. doi:10.2514/3.48441
- [17] Miller, J. C., "Optimally Designed Propellers Constrained by Noise," Ph.D. Thesis, Purdue Univ., Purdue, IN, Dec. 1984.
- [18] Miller, J. C., and Sullivan, J. P., "Noise Constraints Effecting Optimal Propeller Designs," *General Aviation Aircraft Meeting and Exposition*, Society of Automotive Engineers Paper 850871, Wichita, KS, 16–19 Apr. 1985, pp. 4.585–4.593.
- [19] Drack, E. L., and Wood, A. L., "Design and Analysis of Propellers for General Aviation Aircraft Noise Reduction," 21st International Congress of Aeronautical Sciences, Paper 98-5.11.3, Melbourne, Australia, 13–18 Sept. 1998.
- [20] Monk, J. S., "The Aerodynamic Design of an Optimized Propeller for a High Altitude Long Endurance UAV," *23rd International Congress of Aeronautical Sciences*, International Congress of Aeronautical Sciences, 8–13 Sept. 2002, pp. 5104.1–5104.9.
- [21] Gur O., and Rosen, A., "Optimization of Propeller-Based Propulsion System," *Journal of Aircraft*, Vol. 46, No. 1, Jan.–Feb. 2009, pp. 95–106. doi:10.2514/1.36055
- [22] Gur O., and Rosen, A., "Multidisciplinary Design Optimization of a Quiet Propeller," *Journal of Propulsion and Power*, Vol. 25, No. 3, May–June 2009, pp. 717–728. doi:10.2514/1.38814
- [23] Logan, J. M., Chu, J., Motter, A. M., Carter, L. D., Ol, M., and Zeune, C., "Small UAV Research and Evolution in Long Endurance Electric Powered Vehicles," AIAA Infotech @ Aerospace 2007 Conference and Exhibit, AIAA Paper 2007-2730, 7–10 May, 2007.
- [24] Grasmeyer, J. M., and Keennon, M. T., "Development of the Black Widow Micro Air Vehicle," 39th Aerospace Sciences Meeting and Exhibit, AIAA Paper 2001-0127 Reno, NV, 8–11 Jan. 2001.
- [25] Roberts, C., Vaughan, M., and Bowman, W. J., "Development of a Solar Powered Micro Air Vehicle," *40th Aerospace Science Meeting and Exhibit*, AIAA Paper 2002-0703, Reno, NV, 14–17 Jan. 2002.
- [26] Peterson, B., Erath, B., Henry, K., Lyon, M., Walker, B., Powell, N., Fowkes, K., and Bowman, W. J., "Development of a Micro Air Vehicle for Maximum Endurance and Minimum Size," 41st Aerospace Science Meeting and Exhibit, AIAA Paper 2003-416, Reno, NV, 6–9 Jan. 2003.
- [27] Wu, H., Sun, D., and Zhou, Z., "Micro Air Vehicle: Configuration, Analysis, Fabrication, and Test," *IEEE/ASME Transactions on*

- Mechatronics*, Vol. 9, No. 1, Mar. 2004.
- [28] Ott, J., and Biezad, D., "Design of a Tube-Launched UAV," 3rd AIAA "Unmanned Unlimited" Technical Conference, Workshop and Exhibit, AIAA Paper 2004-6493, Chicago, 20–23 Sept. 2004.
- [29] Choi, T. P., Soban, D. S., and Mavris, D. N., "Creation of a Design Framework for All-Electric Aircraft Propulsion Architectures," 3rd International Energy Conversion Engineering Conference, AIAA Paper 2005-5549, San Francisco, 15–18 Aug. 2005.
- [30] Soban, D. S., and Upton, E., "Design of a UAV to Optimize Use of Fuel Cell Propulsion Technology," AIAA Infotech @ Aerospace 2005 Conference and Exhibit, AIAA Paper 2005-7135, Arlington, VA, 26–29 Sept. 2005.
- [31] Gur, O., and Rosen, A., "Comparison Between Blade-Element Models of Propellers," *The Aeronautical Journal*, Vol. 112, No. 1138, Dec. 2008, pp. 689–704.
- [32] Gur, O., and Rosen, A., "Propeller Performance at Low Advance Ratio," *Journal of Aircraft*, Vol. 42, No. 2, Mar.–Apr. 2005, pp. 435–441.
doi:10.2514/1.6564
- [33] Yamamoto, O., and August, R., "Structural and Aerodynamic Analysis of a Large-Scale Advanced Propeller Blade," *Journal of Propulsion and Power*, Vol. 8, No. 2, Mar.–Apr. 1992, pp. 367–373.
doi:10.2514/3.23487
- [34] Rosen, A., and Gur, O., "A Transfer Matrix Model for Large Deformations of Curved Rods," *Computers and Structures*, Vol. 87, Nos. 7–8, Apr. 2009, pp. 467–484.
doi:10.1016/j.compstruc.2008.12.014
- [35] Hanselman, D. C., *Brushless Permanent-Magnet Motor Design*, McGraw-Hill, New York, p. 191.
- [36] Lawrence, D. A., and Mohseni, K., "Efficiency Analysis for Long-Duration Electric MAVs," Infotech @ Aerospace, AIAA Paper 2005-7090, Arlington, VA, 26–29 Sept. 2005.
- [37] Su, G.-J., and Adams, D. J., "Multilevel DC Link Inverter for Brushless Permanent Magnet Motors with Very Low Inductance," *IEEE IAS 2001 Annual Meeting*, Vol. 2, Inst. of Electrical and Electronics Engineers, Piscataway, NJ, 2001, pp. 829–834.
- [38] Logan, M. J., Chu, J., Motter, M. A., Carter, D. L., Ol, M., and Zeune, C., "Small UAV Research and Evolution in Long Endurance Electric Powered Vehicles," Infotech @ Aerospace, AIAA Paper 2007-2730 7–10 May 2007.
- [39] Borst, V. H., "Summary of Propeller Design Procedures and Data," Vol. 1, U.S. Army Air Mobility Research and Development Lab. TR 73-34A/B/C, Moffett Field, CA, Nov. 1973.
- [40] Korkan, K. D., Camba, J., and Morris, P. M., "Aerodynamic Data Banks for Clark-Y, NACA 4-Digit, and NACA 16-Series Airfoil Families," NASA CR 176883, Jan. 1986.
- [41] Boyd, S., and Vandenberghe, L., *Convex Optimization*, Cambridge Univ. Press, New York, 2004, p. 716.
- [42] Goldberg, E. D., *Genetic Algorithms in Search, Optimization, and Machine Learning*, Addison-Wesley, Reading, MA, 1989, p. 412.
- [43] Nelder, J. A., and Mead, R., "A Simplex Method for Function Minimization," *Computer Journal*, Vol. 7, 1965, pp. 308–313.
- [44] Van der Velden, A., "Tools for Applied Engineering Optimization," AGARD Rept. R-803, Neuilly-sur-Seine, France, Apr. 1994.
- [45] Sullivan, J. P., Chang, L. K., and Miller, C. J., "The Effect of Propellers and Bi-Blades on the Performance and Noise of Propellers," SAE Business Aircraft Meeting and Exposition, Society of Automotive Engineers Paper 810600, Wichita, KS, 7–10 Apr. 1981.
- [46] Glauert, H., "Airplane Propellers," *Aerodynamic Theory*, Vol. 4, edited by F. W. Durand, 3rd ed., Dover, New York, 1963.
- [47] Burke, K. A., and Jakupca, I., "Unitized Regenerative Fuel Cell System Gas Storage-Radiator Development," NASA TM 2005-213442, Sept. 2005.
- [48] Wicke, G. B., "General Motors Hydrogen Storage Requirements for Fuel Cell Vehicles," *DOE Hydrogen Storage Workshop*, Argonne National Lab., Argonne, IL, Aug. 2002, http://www1.eere.energy.gov/hydrogenandfuelcells/pdfs/h2_fuelcell_vehicles.pdf [retrieved Mar. 2009].